ACSNANO
www.acsnano.org
ARTICLE

Green Fabrication of Silkworm Cocoon-like Silicon-Based Composite for High-Performance Li-Ion Batteries

Fei-Hu Du,[†] Yizhou Ni,[§] Ye Wang,[†] Dong Wang,[‡] Qi Ge,[‡] Shuo Chen,[§] and Hui Ying Yang*,[†]

[†]Pillar of Engineering Product Development and [‡]Digital Manufacturing and Design Centre, Singapore University of Technology and Design, 8 Somapah Road, Singapore 487372

[§]Department of Physics and Texas Center for Superconductivity, University of Houston, 4800 Calhoun Road, Houston, Texas 77204, United States

Supporting Information

ABSTRACT: **Designing yolk−shell nanostructures is an effective way of addressing the huge volume expansion issue for large-capacity anode and cathode materials in Li-ion batteries (LIBs). Previous studies mainly focused on adopting a SiO_2 template through HF etching to create yolk−shell nanostructures. However, HF etching is highly corrosive and may result in a significant reduction of Si content in the composite. Herein, a silkworm cocoon-like silicon-based composite is prepared through a green approach in which Al_2O_3 was selected as a sacrificial template. The void space between the outer nitrogen-doped carbon (NC) shell formed by chemical vapor deposition using a pyridine precursor and the inside porous silicon nanorods (p-Si NRs) synthesized by magnesiothermic reduction of ordered mesoporous silica nanorods can be generated by etching Al_2O_3 with diluted HCl. The obtained p-Si NRs@void@NC composite is utilized as an anode material for LIBs, which exhibits a large initial discharge capacity of 3161 mAh g^{-1} at 0.5 A g^{-1}, excellent cycling behavior up to 300 cycles, and super rate performance. Furthermore, a deep understanding of the mechanism for the yolk−shell nanostructure during the Li-alloying process is revealed by *in situ* transmission electron microscopy and finite element simulation.**

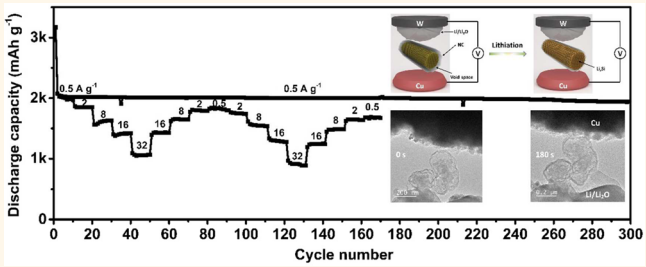

KEYWORDS: *Li-ion batteries, yolk−shell nanostructure, porous silicon nanorods, Al_2O_3 template, in situ transmission electron microscopy, finite element simulation*

Silicon is one of the most hopeful alternative anode materials to commercial graphite for Li-ion batteries (LIBs) owing to its attractive characteristics, such as low discharge potential, unparalleled theoretical capacity, environment-friendly nature, and natural abundance.[1,2] Unfortunately, the huge volume change during the Li-insertion process causes serious cracking of Si, the generation of an uneven solid electrolyte interphase (SEI) film on the Si surface, and electrical disconnection between the Si and current collector, consequently resulting in quick capacity fade.[3−5] Furthermore, the slow Li penetration kinetics in Si and the poor electrical conductivity of Si remarkably limit electrochemical performance of the electrodes.[6] These challenging problems make Si anode material unrealistic for practical applications.

Two main strategies have been adopted for improving the electrochemical property of Si anode materials. One strategy is to exploit various Si nanostructures, such as thin films,[7,8] nanowires,[9,10] nanosheets,[11] nanotubes,[12,13] nanorods,[14] hollow nanospheres,[15] and porous structures.[16,17] Si nanostructures possess evident superiority over bulk Si. However, complicated processes, harsh reaction conditions, and high-cost raw materials are generally used in the fabrication of the above-mentioned Si nanostructures. In 2007, Bao *et al.* reported a simple method to synthesize microporous Si by using diatom frustules *via* a magnesiothermic reduction process.[18] Since then, silica nanosheets,[19] nanotubes,[20] nanofibers,[21] hollow nanospheres,[22,23] and highly ordered mesoporous silica (MCM-41,[24] KIT-6,[25] and SBA-15[26]) have served as both the silicon sources and templates to generate Si nanostructures by the same method. Another strategy is based on the introduction of conductive species including metal nanoparticles,[27,28] carbonaceous matrixes,[29−32] and polymers[33,34] to silicon nanoparticles (NPs). The Si NPs-based composites have several advantages over bare Si NPs. Recently, yolk−shell nanostructures have attracted much

Received: May 31, 2017
Accepted: August 11, 2017
Published: August 11, 2017

DOI: 10.1021/acsnano.7b03830
ACS Nano 2017, 11, 8628−8635

attention for further enhancing the performance of Si NPs-based composites.[35,36] For example, a Si NPs@void@C composite was synthesized by using SiO_2 as a sacrificial template, delivering a specific capacity of about 1200 mAh g^{-1} at 1 C after 1000 cycles.[35] Additionally, a pomegranate-like Si NPs@C composite prepared by the same approach achieved a specific capacity of approximately 1160 mAh g^{-1} at 0.5 C after 1000 cycles.[36] Although these composites have excellent electrochemical characteristics, the process involving HF to etch SiO_2 is environmentally unfriendly and may cause a significant reduction of Si content in the composite. More recently, a granadilla-like Si NPs@C composite was fabricated by using $CaCO_3$ as a hard template.[5] Diluted HCl instead of HF was used to remove the template to generate the yolk−shell nanostructure. Nevertheless, the electrochemical performance of the composite remained unsatisfactory due to uneven dispersion of Si NPs in the matrix and extremely low Si content.

Herein we report a facile strategy for the preparation of a silkworm cocoon-like silicon-based composite using Al_2O_3 as a hard template. The void space between the porous silicon nanorod (p-Si NR) core fabricated *via* magnesiothermic reduction and the nitrogen-doped carbon (NC) shell formed through chemical vapor deposition (CVD) can be generated by etching the template with diluted HCl. The obtained p-Si NRs@void@NC composite shows a much enhanced electrochemical performance compared with the bare p-Si NRs and p-Si NRs@NC composite as the anode material for LIBs. The outstanding performance of the composite is ascribed to a synergistic action of the nanostructured Si core, mechanically strong and highly conductive NC shell, and yolk−shell nanostructure during cycling. *In situ* transmission electron microscopy and finite element simulation are introduced to confirm the advantage of the yolk−shell nanostructure during the lithiation process of the composite.

RESULTS AND DISCUSSION

Materials Synthesis and Characterization. The synthesis process for the p-Si NRs@void@NC composite is illustrated in Figure 1A. Si nanostructures are usually prepared by CVD using toxic and dangerous SiH_4 and by etching of a Si wafer using corrosive HF. To enable a large-scale production of nanostructured Si for possible use in LIBs, we develop a simple magnesiothermic reduction method using mesoporous silica nanorods (m-SiO_2 NRs) as a template and Si source. Uniform m-SiO_2 NRs were prepared by incubating the SiO_2 NRs generated *via* a surfactant-templated approach in water. Scanning electron microscopy (SEM) and transmission electron microscopy (TEM) images (Figure 1B,E) demonstrate that the silica is uniform and rod-like, possessing an average width of 140 nm and length of 420 nm. A high-magnification TEM image (inset of Figure 1E) reveals that the SiO_2 NRs have ordered and radially oriented mesochannels. Three diffraction peaks in a low-angle X-ray diffraction (XRD) pattern of the SiO_2 NRs (Figure S1A) can be regarded as the (100), (110), and (200) reflections related to *p6 mm* hexagonal symmetry, suggesting a well-ordered mesostructure. The nitrogen adsorption−desorption isotherm of the SiO_2 NRs (Figure S1B) shows a characteristic type IV curve, indicating a uniform mesopore architecture. The Brunauer−Emmett−Teller (BET) surface area of the m-SiO_2 NRs is about 1258 m^2 g^{-1}, and the Barrett−Joyner−Halenda (BJH) pore size distribution is around 3.0 nm in diameter. After magnesiothermic reduction and acid washing, the as-made product recorded by high-angle XRD pattern (Figure 2A) is a

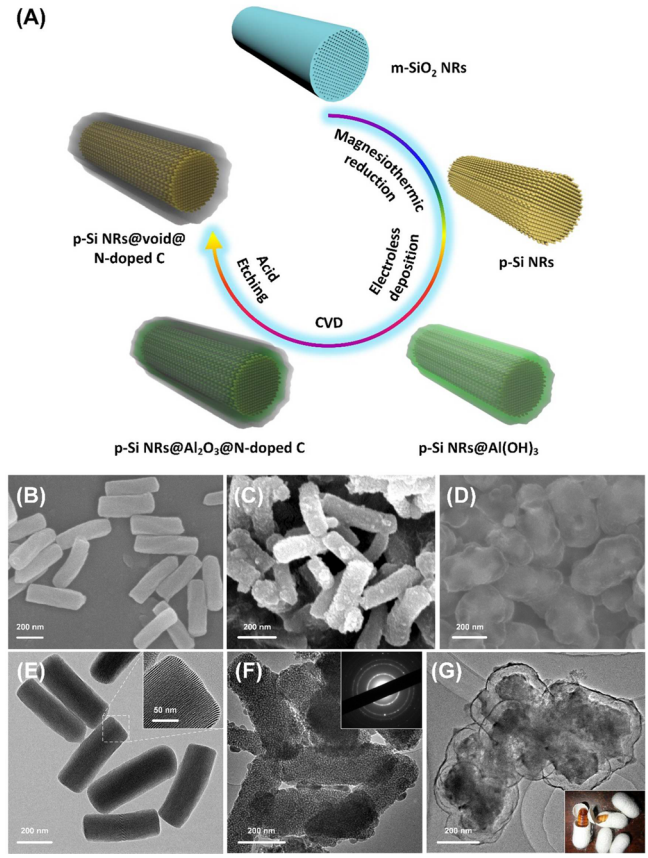

Figure 1. (A) Schematic illustration of the synthesis process for a p-Si NRs@void@NC composite. (B−D) FESEM images of (B) m-SiO_2 NRs, (C) p-Si NRs, and (D) the p-Si NRs@void@NC composite. (E) TEM image of m-SiO_2 NRs, indicating ordered and radially oriented mesochannels (inset). (F) TEM image of p-Si NRs. The inset shows its SAED pattern. (G) TEM image of the p-Si NRs@void@NC composite, showing a silkworm cocoon-like morphology (inset).

cubic phase (JCPDS card No. 27-1402), suggesting the successful conversion of SiO_2 to crystalline Si. The Raman spectra of the product (Figure 2B) show that the strong peak centered at 513 cm^{-1} is attributed to the first-order optical phonon scattering of Si. Furthermore, one broad peak at 294 cm^{-1} is due to scattering of two transverse acoustic phonons, while another peak at 948 cm^{-1} is ascribed to two transverse optical phonons.[23,24] The SEM image (Figure 1C) displays that the shape of the Si is mostly retained as that of the m-SiO_2 NRs. The TEM image (Figure 1F) demonstrates that the Si NRs are composed of 10−15 nm sized Si crystallites, having a porous structure. The diffraction rings in the selected area electron diffraction (SAED) pattern belong to Si (111), (220), and (311) planes, suggesting the polycrystalline nature of the p-Si NRs (inset of Figure 1F). Moreover, the surface area and pore size distribution of the p-Si NRs are about 166 m^2 g^{-1} and 15.2 nm, respectively (Figure 2D).

Al_2O_3 is usually coated on the Si surface by atomic and molecular layer deposition techniques.[37−39] However, these methods are known to be very expensive and tedious. In this work, a layer of $Al(OH)_3$ is generated on the surface of p-Si NRs by a facile method.[40] The coating thickness of $Al(OH)_3$ determines the size of the internal void space, which is critical to retain the structural integrity of the Si anode during the lithiation process. Insufficient space will cause the cracking of the

DOI: 10.1021/acsnano.7b03830
ACS Nano 2017, 11, 8628−8635

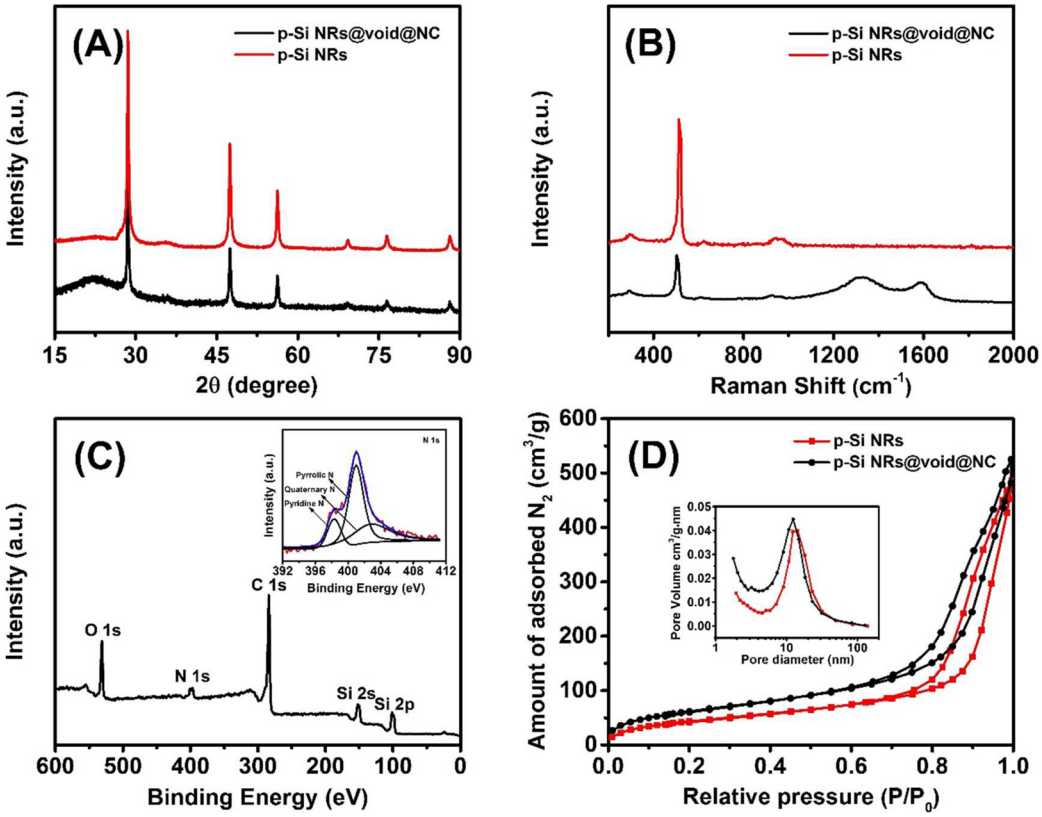

Figure 2. (A) XRD patterns and (B) Raman spectra of the p-Si NRs@void@NC composite and p-Si NRs. (C) XPS survey and HR-XPS N 1s spectra (inset) of the p-Si NRs@void@NC composite. (D) Nitrogen adsorption−desorption isotherms and the corresponding pore size distribution curves (inset) of the p-Si NRs@void@NC composite and p-Si NRs.

conductive shell, whereas too much space will prevent contact between the Si core and shell. Thus, the usage of $Al_2(SO_4)_3$ should be roughly calculated before the experiment (Note S1). FESEM and TEM images (Figure S2) show that the $Al(OH)_3$ layer is successfully grown on the Si NRs surface. The as-prepared p-Si NRs@$Al(OH)_3$ composite is further coated with NCs by CVD using pyridine as the nitrogen and carbon sources. It is noticeable that $Al(OH)_3$ may be decomposed to γ-Al_2O_3 or even α-Al_2O_3 at high temperature. If α-Al_2O_3 is formed, it cannot be etched by diluted HCl. Therefore, the XRD result of the p-Si NRs@Al_2O_3@NC composite shows the amorphous nature of Al_2O_3 (Figure S3). The SEM image (Figure S4A) reveals that the obtained p-Si NRs@Al_2O_3@NC composite still possesses a uniform rod-like shape. The TEM image (Figure S4B) shows double layers without obvious lattice fringes on the Si surface, suggesting the amorphous nature of Al_2O_3 and NC. Further analysis by energy dispersive X-ray (EDX) indicates that the composite consists of Al, C, N, Si, and O elements (Figure S4C). Elemental mappings in the dark field scanning TEM (STEM) image clearly show uniform and continuous coatings of Al_2O_3 and NC throughout the p-Si NRs (Figure S4D,E). After HCl treatment, the obtained p-Si NRs@void@NC composite has an interesting silkworm cocoon-like morphology (inset of Figure 1G), in which every single p-Si NR is wrapped by one hollow NC nanorod with a 40 nm thickness of void space between the Si core and NC shell (Figure 1D,G). The hollow NC NRs remain structurally stable even after complete removal of Si by NaOH aqueous solution (Figure S5). Compared with that of bare p-Si NRs, the XRD result of the p-Si NRs@void@NC composite shows an additional broad peak between 20° and 25°, corresponding to the amorphous NC in the composite (Figure 2A). The Raman result of the composite displays two additional peaks located at 1329 and 1585 cm^{-1}, attributed to the D and G bands of carbon, respectively.[3,24] The intensity ratio of D to G is about 1.1, suggesting that plenty of defects exist in the NC (Figure 2B). The full survey X-ray photoelectron spectroscopy (XPS) scan shows the N, C, Si, and O elements in the p-Si NRs@void@NC composite (Figure 2C). The N content in the composite is about 6.7 at. %. At high resolution the N 1s spectrum has three deconvoluted peaks at 401.2, 399.9, and 398.2 eV, ascribed respectively to quaternary, pyrrolic, and pyridinic nitrogen (inset of Figure 2C). The Raman and XPS results also demonstrate that the NC shell has high electrical conductivity. The surface area and pore size of the p-Si NRs@void@NC composite are approximately 230 $m^2\ g^{-1}$ and 12.0 nm, respectively (Figure 2D). The surface area of the composite is larger than that of the p-Si NRs, indicating that the NC modification contributes to the improvement. The mass content of NC in the composite is about 21.7% as determined by thermogravimetric analysis (TGA) (Figure S6).

Electrochemical Performance. Figure 3A shows cyclic voltammetry (CV) curves of the p-Si NRs@void@NC composite at a scanning rate of 0.1 mV s^{-1}. In the first cycle, there are two peaks located at 0.70 and 0.01 V during discharge, attributed to the generation of an SEI film and Li-alloying reaction, respectively. In the second and third cycles, there are cathodic peaks located at 0.01 and 0.22 V and anodic peaks at 0.34 and 0.51 V, ascribed to two complete lithiation/delithiation processes.[41] Furthermore, the intensity of the anodic and cathodic peaks gradually increases with the cycles, suggesting an activation process of the composite. Figure 3B shows the galvanostatic charge−discharge profiles of the p-Si NRs@void@

DOI: 10.1021/acsnano.7b03830
ACS Nano 2017, 11, 8628−8635

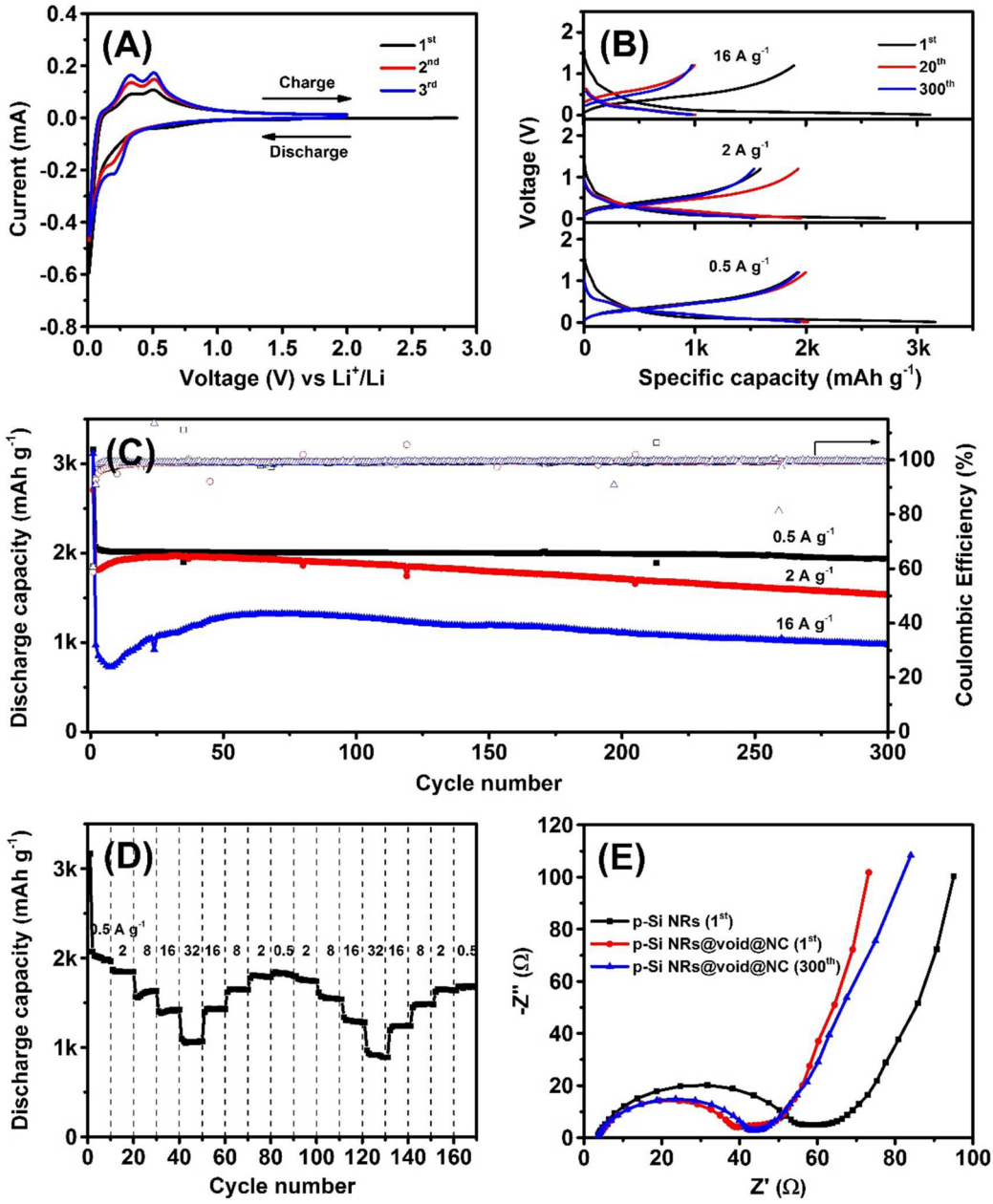

Figure 3. Electrochemical performance of the p-Si NRs@void@NC composite electrode. (A) CV curves at a scanning rate of 0.1 mV s^{-1}. (B) Galvanostatic charge−discharge voltage profiles in the 0.01−1.2 V window for the 1st, 20th, and 300th cycles at 0.5, 2, and 16 A g^{-1}. (C) Cycling performance and CEs at 0.5, 2, and 16 A g^{-1} for 300 cycles. (D) Rate capability at different current densities. (E) Nyquist plots of the p-Si NRs@void@NC composite and bare p-Si NRs electrodes after cycling at 0.5 A g^{-1}.

NC composite in the 0.01−1.2 V window for the first, 20th, and 300th cycles at 0.5, 2, and 16 A g^{-1}. Remarkably, when cycled at a high current density of 16.0 A g^{-1}, the composite should be activated at 0.5 A g^{-1} for the first cycle. First discharge profiles show long plateaus below 0.1 V due to the lithiation processes of crystalline Si. Afterward, the charge−discharge profiles demonstrate the features of amorphous Si. The first discharge capacities of the composite are 3161 mAh g^{-1} at 0.5 A g^{-1} and 2708 mAh g^{-1} at 2 A g^{-1}, respectively, giving Coulombic efficiencies (CEs) of 60.7% and 58.8%. The first capacity loss is attributed to the irreversible Li-alloying reaction and to decomposition of the electrolyte, generating an SEI film on the electrode surface.[42]

The cycling performance of the p-Si NRs@void@NC composite is evaluated at 0.5, 2, and 16 A g^{-1} (Figure 3C). The discharge capacities of the electrode reach 1941 mAh g^{-1} at 0.5 A g^{-1}, 1539 mAh g^{-1} at 2 A g^{-1}, and 978 mAh g^{-1} at 16 A g^{-1} after 300 cycles, which correspond to 93.6%, 84.9%, and 100.0% of its capacity at the second cycle, respectively. We note that the capacities increase slightly in the first several cycles at 2 and 16 A g^{-1}. The possible reason for this phenomenon is due to the gradual activation of the composite, consistent with the CV result. It has been reported that the Si core is gradually exposed during the lithiation process, contributing to the capacity increases.[43] Moreover, CEs of over 97% are well maintained after the fifth cycle at 0.5, 2, and 16 A g^{-1}. However, the p-Si NRs@NC composite and bare p-Si NRs present capacity retentions of only 84.7% and 41.8% at the 100th cycle compared to those at the second cycle, although they can achieve high first

DOI: 10.1021/acsnano.7b03830
ACS Nano 2017, 11, 8628−8635

discharge capacities of 3093 and 3248 mAh g^{-1}, respectively (Figure S7A). The excellent cycling behavior of the p-Si NRs@void@NC composite is due to a synergistic action of the nanostructured Si core, mechanically strong NC shell, and yolk−shell nanostructure. The porous structure of Si acting as a cushion can partially release the mechanical stress and offer the volume expansion. The mechanically strong shell can limit the volume change and reduce the contact between the Si surface and electrolyte, preventing the generation of an uneven SEI film. The yolk−shell nanostructure can provide internal void space, which makes expansion of Si occur freely during lithiation without damaging the outer shell.

Figure 3D shows the rate performance of the p-Si NRs@void@NC composite. It can achieve discharge capacities of 3170, 1867, 1565, 1404, and 1093 mAh g^{-1} at 0.5, 2, 8, 16, and 32 A g^{-1}, respectively. It is interesting to find that the voltage plateaus of these discharge curves are around 0.19 V (Figure S8), higher than that of the reported graphite and Si NPs.[26] The high Li^+ intercalation potential may restrain the generation of metallic Li or Li dendrites, preventing explosion accidents in real battery usage. The composite can deliver a discharge capacity of 1640 mAh g^{-1} when the current density is adjusted step by step again from 32 to 0.5 A g^{-1}, demonstrating its repeatable rate capability. However, low discharge capacities of 1048 and 853 mAh g^{-1} are retained for the p-Si NRs@NC composite and bare p-Si NRs when the current density is adjusted step by step from 0.5 to 32 A g^{-1}, respectively (Figure S7B). The high rate performance of the p-Si NRs@void@NC is attributed to a synergistic action of the nanostructured Si core, highly conductive NC shell, and yolk−shell nanostructure. The porous structure of the Si and void space in the composite can shorten the penetration length of Li^+ and the electrolyte into the electrode. The NC shell can enhance the electrical conductivity of the electrode, offering an effective electron transport channel from the current collector to the p-Si NRs.

Figure 3E shows the electrochemical impedance spectroscopy (EIS) curves for the p-Si NRs@void@NC composite and bare p-Si NRs electrodes after cycling at 0.5 A g^{-1}. With the incorporation of NC into the p-Si NRs, the resistance of the composite electrode is much lower than that of the bare p-Si NRs after the first cycle. In addition, no obvious enhancement of composite resistance is observed after 300 cycles, indicating that there is no excess SEI film growth. Cross-sectional FESEM images (Figure 4A,B) show that the NC cage's built-in void space prevents a large change in electrode thickness (only 24% change in thickness), allowing the composite to maintain electrical contact on the electrode level. However, without NC modification, the bare p-Si NRs become electrically disconnected from each other, leading to a catastrophic electrode swelling by over 150% (Figure S9A,B). The top-view FESEM image (Figure 4C) shows that the composite electrode remains stable and without fracture after cycling. The magnified FESEM image (Figure 4D) shows no apparent cracking of p-Si NRs and detachment of the NC shell. Furthermore, the TEM image (Figure 4E) displays that almost all void space is occupied by Si after cycling. Nevertheless, the bare p-Si NR electrode has several cracks, and it is difficult to recognize the morphology of the p-Si NRs after cycling (Figure S9C−E).

To confirm the advantage of the yolk−shell nanostructure, *in situ* TEM was introduced to investigate the lithiation processes of p-Si NRs@NC and p-Si NRs@void@NC composites. The *in situ* TEM setup is shown schematically in Figure 5A. The technique allows us to directly observe silicon's volume expansion and

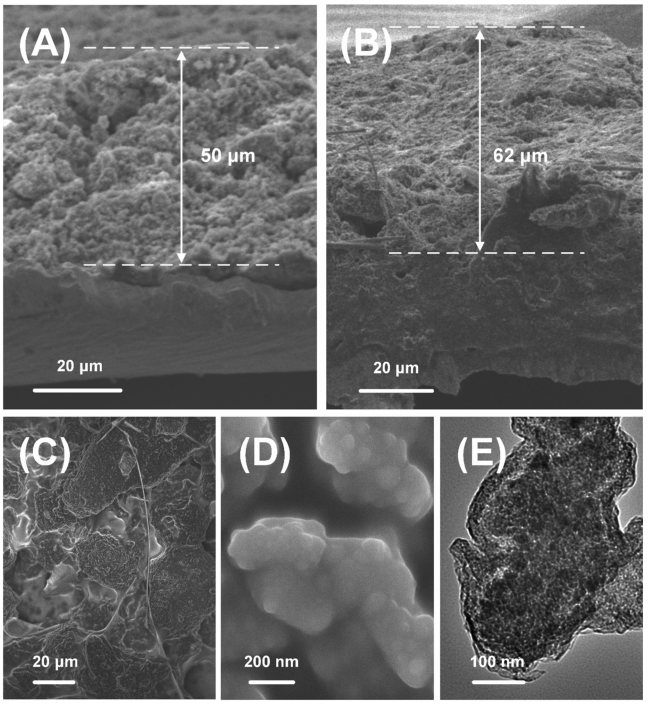

Figure 4. (A, B) Cross-sectional FESEM images of the p-Si NRs@void@NC composite electrode (A) before and (B) after 300 cycles at 0.5 A g^{-1}. (C, D) Top-view FESEM and (E) TEM images of the p-Si NRs@void@NC composite electrode after 300 cycles at 0.5 A g^{-1}.

particle fracture during battery operation. Figure 5B−D demonstrate the images intercepted from a video of the *in situ* lithiation of the p-Si NRs@void@NC composite (Video S1). The p-Si NR is visible within a surrounding NC shell before lithiation (Figure 5B). Then, the particle expands in volume as Li^+ permeates through the NC and alloys with Si. The particle is partially lithiated after 90 s (Figure 5C). After 3 min, almost all void space is occupied by lithiated p-Si NR, and no fracture of the NC shell is observed after full lithiation (Figure 5D). For the p-Si NRs@NC composite, however, the NC shell is broken by the expansion of the p-Si NR, and finally the whole morphology is damaged (Figure 5E−G and Video S2). All these results indicate that the yolk−shell nanostructure possessing internal void space makes expansion of the p-Si NRs occur freely without destroying the NC shell, effectively preventing the battery anode from changing structurally and thus enhancing the cycle life.

Simulation. Finite element (FE) analysis was performed to further confirm the advantage of the yolk−shell nanostructure. The shape of Si can be modeled as a cylinder with a height of 400 nm and radius of 65 nm. The thicknesses of the NC shell and void space for the p-Si NRs@void@NC composite are 10 and 40 nm, respectively. The thickness of the NC coating layer for the p-Si NRs@NC composite is 10 nm. The Young's modulus and Poisson ratio of lithiated Si are 12 GPa and 0.2, respectively.[44,45] The Young's modulus and Poisson ratio of NC are 950 GPa and 0.2, respectively.[46] The expansion of Si upon complete lithiation is assumed to be 300%.[6] The Si and NC in the numerical model were discretized using the brick element (C3D8R). Because of symmetry, only 1/8 of the whole structure was simulated. In the simulation, the cylinder first contacts the NC shell at the top and bottom faces during the lithiation process and then expands mainly along the width direction due to the constraint of the NC shell. The maximum Mises stress on the NC shell is about 41

DOI: 10.1021/acsnano.7b03830
ACS Nano 2017, 11, 8628−8635

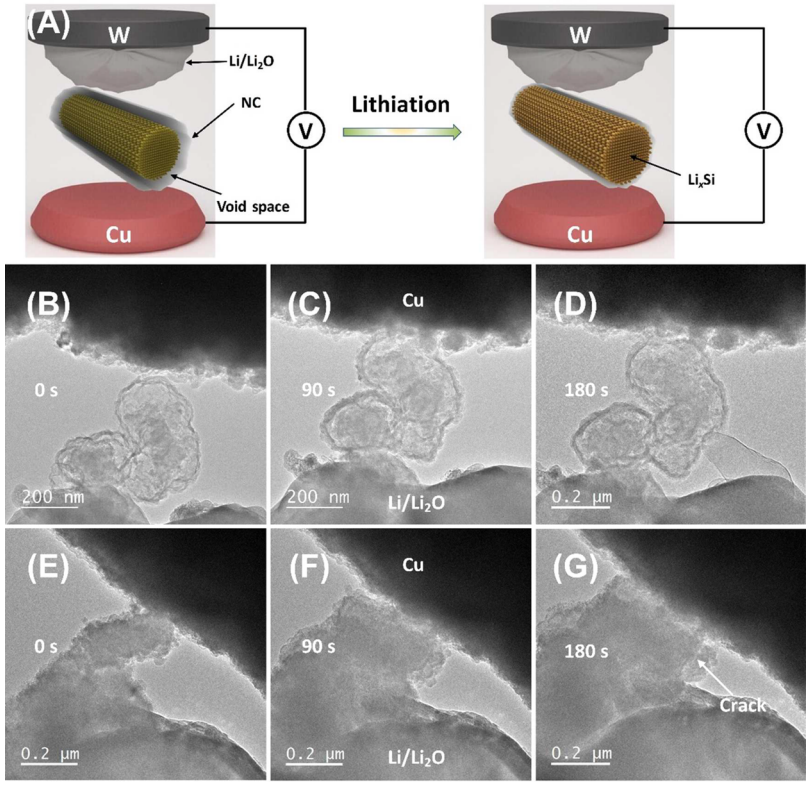

Figure 5. (A) Diagram of the nanoscale electrochemical cell for *in situ* (de)lithiation within the TEM. (B–G) Time-lapse images of the lithiation of (B–D) p-Si NRs@void@NC and (E–G) p-Si NRs@NC composites.

GPa (Figure 6A), which is lower than that (approximately 71 GPa in Figure 6B) on the NC shell directly attached to the Si. As the tensile strength of the NC can reach 63 GPa,[46] the NC in the yolk–shell nanostructure will still be unbroken after lithiation, while that without a yolk–shell nanostructure will fracture. Moreover, it shows clearly that the maximum stresses exist at the corners of the NC (Figure 6C).

CONCLUSION

In summary, a facile method has been exploited for the preparation of a silkworm cocoon-like silicon-based composite using Al_2O_3 as a hard template. Diluted HCl instead of HF was used to remove the template to generate the yolk–shell nanostructure. The resulting p-Si NRs@void@NC composite exhibits a large specific capacity, superior cycling behavior, and high rate performance as an anode material for LIBs. Nanostructured Si can reduce the penetration length of the electrolyte and Li^+ into the electrode and partially offer the large volume expansion. The NC shell can further restrict the volume change, reduce the contact between the p-Si NR surface and electrolyte, and enhance the overall electrical conductivity of the electrode. The yolk–shell nanostructure provides internal void space for free expansion of Si. *In situ* TEM and FE analyses were introduced to confirm the advantage of the yolk–shell nanostructure during the lithiation process of the composite. Therefore, the p-Si NRs@void@NC presented here shows great promise for further mass production as a high-performance composite anode.

METHODS

Synthesis of Mesoporous Silica Nanorods. Typically, tetraethoxysilane (TEOS) (1.42 mL) was slowly dropped into distilled water (100 mL) containing cetyltrimethylammonium bromide (CTAB) (0.58 g) and concentrated ammonia aqueous solution (3.26 mL, 29 wt %) with strong stirring. After reaction at 30 °C for 7 h, the white SiO_2 floccule was filtered and washed with absolute alcohol. The powder was immersed in distilled water (250 mL) at 90 °C for 45 h. The sample obtained by filtration was reimmersed in absolute alcohol (90 mL) containing concentrated hydrochloric acid (10 mL, 37 wt %) and stirred at 60 °C for 20 h to remove the CTAB.

Preparation of p-Si NRs. A mixture of m-SiO_2 NRs (500 mg) and Mg powder (500 mg) was placed in a tube furnace at 650 °C for 6 h under a gas mixture of H_2 and Ar (5:95 v/v). The heating rate was maintained at 4 °C min^{-1}. The resulting powder was dispersed in a 1 M HCl solution for 8 h to remove magnesium oxide.

Fabrication of the p-Si NRs@void@NC Composite. First, the p-Si NRs@$Al(OH)_3$ composite was fabricated according to the literature approach.[40] Typically, formic acid was added to distilled water (100 mL) containing ammonium formate (1.26 g) to reach a pH value of 4.4. Then p-Si NRs (0.05 g) and aluminum sulfate (0.55 g) were dispersed in the above solution and kept at 70 °C for 2 h with strong stirring. The resulting powder was isolated by filtration, washed with alcohol, and vacuum-dried at 70 °C for 12 h. Then, the obtained p-Si NRs@$Al(OH)_3$ composite was heated to 800 °C at a rate of 50 °C min^{-1} under an Ar atmosphere. Pyridine vapor was then carried by Ar gas flow through the bubbling of pyridine for 15 min. Finally, the as-prepared p-Si NRs@Al_2O_3@NC composite was dispersed in a 1 M HCl solution for 10 h to etch the template. The p-Si NRs@NC composite was fabricated without the Al_2O_3 template using the same procedure.

Characterization. The morphology and structure were characterized on a JSM-7401F SEM and a JEM-2100F TEM. Powder XRD patterns were collected on a D8 Advance X-ray diffractometer with Cu Kα radiation. XPS was performed on an AXIS Ultra DLD spectrometer with Al Kα radiation. The Raman spectra were carried out on an Alpha300 confocal Raman microscope. The surface area and pore size distribution were measured on an ASAP 2010 M+C analyzer. TGA was acquired on an SDT Q600 thermoanalyzer in air.

DOI: 10.1021/acsnano.7b03830
ACS Nano 2017, 11, 8628–8635

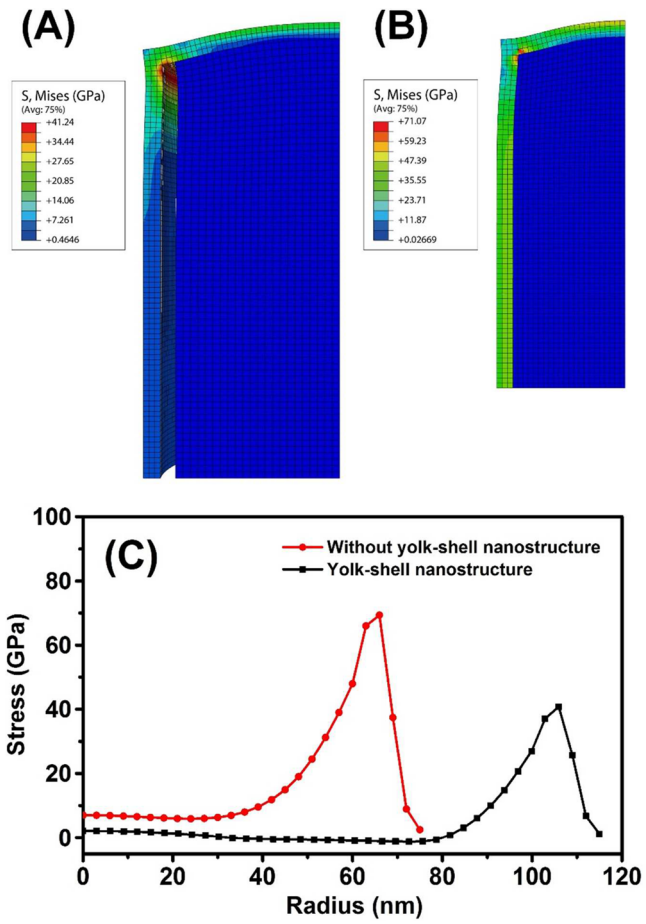

Figure 6. (A, B) Deformed shapes and stress distributions of (A) p-Si NRs@void@NC and (B) p-Si NRs@NC composites after lithiation. (C) Stress distributions in the radius direction of the NC at the top contact face.

***In Situ* TEM.** p-Si NRs@NC and p-Si NRs@void@NC composites were respectively dispersed on the edge of a Cu half-grid. Li metal was attached to a 0.3 mm diameter tungsten (W) wire, and a naturally grown Li_2O layer on the surface of Li acted as the electrolyte. Then the grid and W wire were brought into contact, and a voltage bias of −2 V was applied to force Li^+ to insert into the composite using a TEM manipulator holder (Hummingbird Scientific, USA). The lithiation processes were observed under a JEM-2010F TEM.

Simulation. FE analysis was preformed using the commercial software package ABAQUS (Simulia, Providence, RI, USA).

Electrochemical Measurements. Sodium carboxymethyl cellulose (0.015 g) and sample (0.085 g) were first dispersed in distilled water to obtain a uniform slurry. Then the slurry was coated onto a Cu foil and vacuum-dried at 70 °C overnight. The Cu foil was finally cut into a round shape with a diameter of 12 mm. The cells were assembled in an Ar-filled glovebox using the prepared electrode, Li metal, glass microfiber filter (Whatman, UK), and 1 M $LiPF_6$ in ethyl carbonate/dimethyl carbonate (1:1 v/v) as working electrode, counter electrode, separator, and electrolyte, respectively. The galvanostatic charge and discharge testing was carried out by a battery tester (Neware, China). CV was measured at a scaning rate of 1 mV s^{-1}, and EIS was evaluated in a range of 100 kHz to 10 MHz on an electrochemical workstation (VMP3, Bio-Logic, France). The specific capacity was calculated according to the total mass of the composite including the NC and Si.

ASSOCIATED CONTENT

Supporting Information

The Supporting Information is available free of charge on the ACS Publications website at DOI: 10.1021/acsnano.7b03830.

Theoretical calculation of $Al_2(SO_4)_3$ usage and void space thickness, low-angle XRD pattern and nitrogen adsorption−desorption isotherm and the corresponding pore size distribution curve of m-SiO_2 NRs, high-angle XRD pattern of p-Si NRs@Al_2O_3@NC, morphology and structure of p-Si NRs@$Al(OH)_3$, p-Si NRs@Al_2O_3@NC, and hollow NC NRs, TG curve of p-Si NRs@void@NC, cycling stability and rate capability of p-Si NRs@NC and p-Si NRs electrodes, charge−discharge profiles of p-Si NRs@void@NC at various current densities, and morphology and structure of p-Si electrode before and after cycling (PDF)

Movie 1 (AVI)

Movie 2 (AVI)

AUTHOR INFORMATION

Corresponding Author

*E-mail: yanghuiying@sutd.edu.sg (H. Y. Yang).

ORCID

Hui Ying Yang: 0000-0002-2244-8231

Notes

The authors declare no competing financial interest.

ACKNOWLEDGMENTS

This work is supported by Singapore Ministry of Education Academic Research Fund Tier 2 (MOE2015-T2-1-150) and SUTD Digital Manufacturing and Design (DManD) Center. S.C. and Y.N. appreciate the support from TcSUH as TcSUH Robert A. Welch Professorships on High Temperature Superconducting (HTSg) and Chemical Materials (E-0001). The *in situ* TEM holder acquisition is supported by the Defense University Research Instrumentation Program (FA2386-14-1-3007).

REFERENCES

(1) Wang, K. X.; Li, X. H.; Chen, J. S. Surface and Interface Engineering of Electrode Materials for Lithium-Ion Batteries. *Adv. Mater.* **2015**, *27*, 527−545.

(2) Du, F. H.; Wang, K. X.; Chen, J. S. Strategies to Succeed in Improving the Lithium-Ion Storage Properties of Silicon Nanomaterials. *J. Mater. Chem. A* **2016**, *4*, 32−50.

(3) Du, F. H.; Liu, Y. S.; Long, J.; Zhu, Q. C.; Wang, K. X.; Wei, X.; Chen, J. S. Incorporation of Heterostructured Sn/SnO Nanoparticles in Crumpled Nitrogen-Doped Graphene Nanosheets for Application as Anodes in Lithium-ion Batteries. *Chem. Commun.* **2014**, *50*, 9961−9964.

(4) Wu, H.; Cui, Y. Designing Nanostructured Si Anodes for High Energy Lithium Ion Batteries. *Nano Today* **2012**, *7*, 414−429.

(5) Zhang, L.; Rajagopalan, R.; Guo, H.; Hu, X.; Dou, S.; Liu, H. A Green and Facile Way to Prepare Granadilla-Like Silicon-Based Anode Materials for Li-Ion Batteries. *Adv. Funct. Mater.* **2016**, *26*, 440−446.

(6) Su, X.; Wu, Q.; Li, J.; Xiao, X.; Lott, A.; Lu, W.; Sheldon, B. W.; Wu, J. Silicon-Based Nanomaterials for Lithium-Ion Batteries: A Review. *Adv. Energy Mater.* **2014**, *4*, 1300882.

(7) Graetz, J.; Ahn, C. C.; Yazami, R.; Fultz, B. Highly Reversible Lithium Storage in Nanostructured Silicon. *Electrochem. Solid-State Lett.* **2003**, *6*, A194−A197.

(8) Pereira-Nabais, C.; Swiatowska, J.; Rosso, M.; Ozanam, F.; Seyeux, A.; Gohier, A.; Tran-Van, P.; Cassir, M.; Marcus, P. Effect of Lithiation Potential and Cycling on Chemical and Morphological Evolution of Si

DOI: 10.1021/acsnano.7b03830
ACS Nano 2017, 11, 8628−8635

Thin Film Electrode Studied by ToF-SIMS. *ACS Appl. Mater. Interfaces* **2014**, *6*, 13023−13033.
(9) Chan, C. K.; Peng, H.; Liu, G.; McIlwrath, K.; Zhang, X. F.; Huggins, R. A.; Cui, Y. High-Performance Lithium Battery Anodes Using Silicon Nanowires. *Nat. Nanotechnol.* **2008**, *3*, 31−35.
(10) Peng, K.; Jie, J.; Zhang, W.; Lee, S. T. Silicon Nanowires for Rechargeable Lithium-Ion Battery Anodes. *Appl. Phys. Lett.* **2008**, *93*, 033105.
(11) Yu, X.; Xue, F.; Huang, H.; Liu, C.; Yu, J.; Sun, Y.; Dong, X.; Cao, G.; Jung, Y. Synthesis and Electrochemical Properties of Silicon Nanosheets by DC Arc Discharge for Lithium-Ion Batteries. *Nanoscale* **2014**, *6*, 6860−6865.
(12) Park, M. H.; Kim, M. G.; Joo, J.; Kim, K.; Kim, J.; Ahn, S.; Cui, Y.; Cho, J. Silicon Nanotube Battery Anodes. *Nano Lett.* **2009**, *9*, 3844−3847.
(13) Wu, H.; Chan, G.; Choi, J. W.; Ryu, I.; Yao, Y.; McDowell, M. T.; Lee, S. W.; Jackson, A.; Yang, Y.; Hu, L.; Cui, Y. Stable Cycling of Double-Walled Silicon Nanotube Battery Anodes Through Solid-Electrolyte Interphase Control. *Nat. Nanotechnol.* **2012**, *7*, 310−315.
(14) Hieu, N. S.; Lim, J. C.; Lee, J. K. Free-Standing Silicon Nanorods on Copper Foil as Anode for Lithium-Ion Batteries. *Microelectron. Eng.* **2012**, *89*, 138−140.
(15) Yao, Y.; McDowell, M. T.; Ryu, I.; Wu, H.; Liu, N.; Hu, L.; Nix, W. D.; Cui, Y. Interconnected Silicon Hollow Nanospheres for Lithium-Ion Battery Anodes with Long Cycle Life. *Nano Lett.* **2011**, *11*, 2949−2954.
(16) Ge, M.; Lu, Y.; Ercius, P.; Rong, J.; Fang, X.; Mecklenburg, M.; Zhou, C. Large-Scale Fabrication, 3D Tomography, and Lithium-Ion Battery Application of Porous Silicon. *Nano Lett.* **2014**, *14*, 261−268.
(17) Esmanski, A.; Ozin, G. A. Silicon Inverse-Opal-Based Macroporous Materials as Negative Electrodes for Lithium Ion Batteries. *Adv. Funct. Mater.* **2009**, *19*, 1999−2010.
(18) Bao, Z.; Weatherspoon, M. R.; Shian, S.; Cai, Y.; Graham, P. D.; Allan, S. M.; Ahmad, G.; Dickerson, M. B.; Church, B. C.; Kang, Z.; Abernathy, H. W., III; Summers, C. J.; Liu, M.; Sandhage, K. H. Chemical Reduction of Three-Dimensional Silica Micro-Assemblies into Microporous Silicon Replicas. *Nature* **2007**, *446*, 172−175.
(19) Lu, Z.; Zhu, J.; Sim, D.; Zhou, W.; Shi, W.; Hng, H. H.; Yan, Q. Synthesis of Ultrathin Silicon Nanosheets by Using Graphene Oxide as Template. *Chem. Mater.* **2011**, *23*, 5293−5295.
(20) Yoo, J. K.; Kim, J.; Jung, Y. S.; Kang, K. Scalable Fabrication of Silicon Nanotubes and their Application to Energy Storage. *Adv. Mater.* **2012**, *24*, 5452−5456.
(21) Lee, D. J.; Lee, H.; Ryou, M. H.; Han, G. B.; Lee, J. N.; Song, J.; Choi, J.; Cho, K. Y.; Lee, Y. M.; Park, J. K. Electrospun Three-Dimensional Mesoporous Silicon Nanofibers as an Anode Material for High-Performance Lithium Secondary Batteries. *ACS Appl. Mater. Interfaces* **2013**, *5*, 12005−12010.
(22) Chen, D.; Mei, X.; Ji, G.; Lu, M.; Xie, J.; Lu, J.; Lee, J. Y. Reversible Lithium-Ion Storage in Silver-Treated Nanoscale Hollow Porous Silicon Particles. *Angew. Chem., Int. Ed.* **2012**, *51*, 2409−2413.
(23) Du, F. H.; Li, B.; Fu, W.; Xiong, Y. J.; Wang, K. X.; Chen, J. S. Surface Binding of Polypyrrole on Porous Silicon Hollow Nanospheres for Li-Ion Battery Anodes with High Structure Stability. *Adv. Mater.* **2014**, *26*, 6145−6150.
(24) Du, F. H.; Wang, K. X.; Fu, W.; Gao, P. F.; Wang, J. F.; Yang, J.; Chen, J. S. A Graphene-Wrapped Silver-Porous Silicon Composite with Enhanced Electrochemical Performance for Lithium-Ion Batteries. *J. Mater. Chem. A* **2013**, *1*, 13648−13654.
(25) Gao, P.; Jia, H.; Yang, J.; Nuli, Y.; Wang, J.; Chen, J. Three-Dimensional Porous Silicon-MWNT Heterostructure with Superior Lithium Storage Performance. *Phys. Chem. Chem. Phys.* **2011**, *13*, 20108−20111.
(26) Jia, H.; Gao, P.; Yang, J.; Wang, J.; Nuli, Y.; Yang, Z. Novel Three-Dimensional Mesoporous Silicon for High Power Lithium-Ion Battery Anode Material. *Adv. Energy Mater.* **2011**, *1*, 1036−1039.
(27) Murugesan, S.; Harris, J. T.; Korgel, B. A.; Stevenson, K. J. Copper-Coated Amorphous Silicon Particles as an Anode Material for Lithium-Ion Batteries. *Chem. Mater.* **2012**, *24*, 1306−1315.
(28) Yoo, S.; Lee, J. I.; Ko, S.; Park, S. Highly Dispersive and Electrically Conductive Silver-Coated Si Anodes Synthesized *via* a Simple Chemical Reduction Process. *Nano Energy* **2013**, *2*, 1271−1278.
(29) Magasinski, A.; Dixon, P.; Hertzberg, B.; Kvit, A.; Ayala, J.; Yushin, G. High-Performance Lithium-Ion Anodes Using a Hierarchical Bottom-Up Approach. *Nat. Mater.* **2010**, *9*, 353−358.
(30) Liu, Y.; Huang, K.; Fan, Y.; Zhang, Q.; Sun, F.; Gao, T.; Wang, Z.; Zhong, J. Binder-Free Si Nanoparticles@Carbon Nanofiber Fabric as Energy Storage Material. *Electrochim. Acta* **2013**, *102*, 246−251.
(31) Gohier, A.; Laik, B.; Kim, K. H.; Maurice, J. L.; Pereira-Ramos, J. P.; Cojocaru, C. S.; Van, P. T. High-Rate Capability Silicon Decorated Vertically Aligned Carbon Nanotubes for Li-Ion Batteries. *Adv. Mater.* **2012**, *24*, 2592−2597.
(32) Zhao, X.; Hayner, C. M.; Kung, M. C.; Kung, H. H. In-Plane Vacancy-Enabled High-Power Si-Graphene Composite Electrode for Lithium-Ion Batteries. *Adv. Energy Mater.* **2011**, *1*, 1079−1084.
(33) Wu, H.; Yu, G.; Pan, L.; Liu, N.; McDowell, M. T.; Bao, Z.; Cui, Y. Stable Li-Ion Battery Anodes by *in-situ* Polymerization of Conducting Hydrogel to Conformally Coat Silicon Nanoparticles. *Nat. Commun.* **2013**, *4*, 1943.
(34) Zhou, X. Y.; Tang, J. J.; Yang, J.; Zou, Y. L.; Wang, S. C.; Xie, J.; Ma, L. L. Effect of Polypyrrole on Improving Electrochemical Performance of Silicon Based Anode Materials. *Electrochim. Acta* **2012**, *70*, 296−303.
(35) Liu, N.; Wu, H.; McDowell, M. T.; Yao, Y.; Wang, C.; Cui, Y. A Yolk-Shell Design for Stabilized and Scalable Li-Ion Battery Alloy Anodes. *Nano Lett.* **2012**, *12*, 3315−3321.
(36) Liu, N.; Lu, Z.; Zhao, J.; McDowell, M. T.; Lee, H. W.; Zhao, W.; Cui, Y. A Pomegranate-Inspired Nanoscale Design for Large-Volume-Change Lithium Battery Anodes. *Nat. Nanotechnol.* **2014**, *9*, 187−192.
(37) Xiao, X.; Lu, P.; Ahn, D. Ultrathin Multifunctional Oxide Coatings for Lithium Ion Batteries. *Adv. Mater.* **2011**, *23*, 3911−3915.
(38) Lotfabad, E. M.; Kalisvaart, P.; Kohandehghan, A.; Cui, K.; Kupsta, M.; Farbod, B.; Mitlin, D. Si Nanotubes ALD Coated with TiO_2, TiN or Al_2O_3 as High Performance Lithium Ion Battery Anodes. *J. Mater. Chem. A* **2014**, *2*, 2504−2516.
(39) Luo, L.; Yang, H.; Yan, P.; Travis, J. J.; Lee, Y.; Liu, N.; Piper, D. M.; Lee, S. H.; Zhao, P.; George, S. M.; Zhang, J. G.; Cui, Y.; Zhang, S.; Ban, C.; Wang, C. M. Surface-Coating Regulated Lithiation Kinetics and Degradation in Silicon Nanowires for Lithium Ion Battery. *ACS Nano* **2015**, *9*, 5559−5566.
(40) Zhang, W.; Chi, Z. X.; Mao, W. X.; Lv, R. W.; Cao, A. M.; Wan, L. J. One-Nanometer-Precision Control of Al_2O_3 Nanoshells through a Solution-Based Synthesis Route. *Angew. Chem., Int. Ed.* **2014**, *53*, 12776−12780.
(41) Shen, X.; Jiang, W.; Sun, H.; Wang, Y.; Dong, A.; Hu, J.; Yang, D. Ionic Liquid Assist to Prepare Si@N-Doped Carbon Nanoparticles and Its High Performance in Lithium Ion Batteries. *J. Alloys Compd.* **2017**, *691*, 178−184.
(42) Yu, Y.; Gu, L.; Zhu, C.; Tsukimoto, S.; van Aken, P. A.; Maier, J. Reversible Storage of Lithium in Silver-Coated Three-Dimensional Macroporous Silicon. *Adv. Mater.* **2010**, *22*, 2247−2250.
(43) Liu, X. H.; Fan, F.; Yang, H.; Zhang, S.; Huang, J. Y.; Zhu, T. Self-Limiting Lithiation in Silicon Nanowires. *ACS Nano* **2013**, *7*, 1495−1503.
(44) Zhao, K.; Pharr, M.; Hartle, L.; Vlassak, J. J.; Suo, Z. Fracture and Debonding in Lithium-Ion Batteries with Electrodes of Hollow Core-Shell Nanostructures. *J. Power Sources* **2012**, *218*, 6−14.
(45) Ryu, I.; Lee, S. W.; Gao, H.; Cui, Y.; Nix, W. D. Microscopic Model for Fracture of Crystalline Si Nanopillars during Lithiation. *J. Power Sources* **2014**, *255*, 274−282.
(46) Yu, M. F.; Lourie, O.; Dyer, M. J.; Moloni, K.; Kelly, T. F.; Ruoff, R. S. Strength and Breaking Mechanism of Multiwalled Carbon Nanotubes under Tensile Load. *Science* **2000**, *287*, 637−640.

DOI: 10.1021/acsnano.7b03830
ACS Nano 2017, 11, 8628−8635